

# Constrained Dynamic Gaussian Splatting

Zihan Zheng, Zhenlong Wu, Xuanxuan Wang, Houqiang Zhong, Xiaoyun Zhang, *Member, IEEE*,  
 Qiang Hu, *Member, IEEE*, Guangtao Zhai, *Fellow, IEEE*, Wenjun Zhang, *Fellow, IEEE*

**Abstract**—While Dynamic Gaussian Splatting enables high-fidelity 4D reconstruction, its deployment is severely hindered by a fundamental dilemma: unconstrained densification leads to excessive memory consumption incompatible with edge devices, whereas heuristic pruning fails to achieve optimal rendering quality under preset Gaussian budgets. In this work, we propose Constrained Dynamic Gaussian Splatting (CDGS), a novel framework that formulates dynamic scene reconstruction as a budget-constrained optimization problem to enforce a strict, user-defined Gaussian budget during training. Our key insight is to introduce a differentiable budget controller as the core optimization driver. Guided by a multi-modal unified importance score, this controller fuses geometric, motion, and perceptual cues for precise capacity regulation. To maximize the utility of this fixed budget, we further decouple the optimization of static and dynamic elements, employing an adaptive allocation mechanism that dynamically distributes capacity based on motion complexity. Furthermore, we implement a three-phase training strategy to seamlessly integrate these constraints, ensuring precise adherence to the target count. Coupled with a dual-mode hybrid compression scheme, CDGS not only strictly adheres to hardware constraints (error <2%) but also pushes the Pareto frontier of rate-distortion performance. Extensive experiments demonstrate that CDGS delivers optimal rendering quality under varying capacity limits, achieving over 3x compression compared to state-of-the-art methods.

**Index Terms**—Dynamic Gaussian Splatting, Neural Rendering, Resource-Constrained Rendering, Immersive Media.

## I. INTRODUCTION

Free-viewpoint Video (FVV) enables users to freely and dynamically explore 3D scenes from arbitrary viewpoints, revolutionizing immersive media experiences in VR/AR, sports broadcasting, and telepresence. While offering unprecedented interactivity, the mass deployment of FVV is severely bottlenecked by the heterogeneity of end-user hardware. The strict memory and bandwidth limitations of edge devices stand in sharp contrast to the massive data requirements of high-fidelity volumetric content, making it crucial to maximize reconstruction quality under strict resource constraints.

Early methods for FVV reconstruction typically employed dynamic meshes [1], [2], point clouds [3]–[5], depth maps [6], [7] or image-based view interpolation [8], frequently resulting in compromised visual quality, especially in complex dynamic scenes. Neural Radiance Fields (NeRF) [9] and its variants [10]–[15] marked a breakthrough in novel view synthesis. Subsequent work on dynamic NeRF [16]–[20] extensions incorporating temporal modeling further expanded FVV’s potential. However, practical deployment remains challenging due

Zihan Zheng, Zhenglong Wu, Xuanxuan Wang, Houqiang Zhong, Xiaoyun Zhang, Qiang Hu, Guangtao Zhai and Wenjun Zhang are with the Shanghai Jiao Tong University, Shanghai, 200240, China. (email: {1364406834, 1821863716, wangxuanxuan, zhonghouqiang, xiaoyun.zhang, qiang.hu, zhaiguangtao, zhangwenjun}@sjtu.edu.cn).

to slow rendering, inconsistent output quality, and substantial computational requirements.

Recently, 3D Gaussian Splatting (3DGS) [24] has revolutionized real-time rendering. However, dynamic extensions [21]–[23], [25] typically struggle with explosive growth in Gaussian counts, where unconstrained densification defies hardware limits. While recent advancements attempt to address efficiency, they fail to simultaneously achieve controllability and optimal allocation. For instance, Ex4DGS [23] reduces redundancy via decomposition but lacks explicit capacity control, relying on heuristics that yield unpredictable model complexity. Conversely, methods like Taming 3DGS [26] introduce budget control but are restricted to static scenes. More critically, they enforce limits via rigid pruning rather than integrating the budget constraint directly into the training loop as a differentiable objective. Consequently, the optimization trajectory remains unaware of the capacity limit, leading to suboptimal convergence. Furthermore, applying such static strategies to dynamic settings proves inadequate: relying solely on static geometric metrics leads to an incomplete assessment of primitive importance, as it fails to account for kinematic significance and thus cannot effectively preserve transient, high-frequency motion details. Our key insight is that optimal constrained reconstruction requires integrating the budget directly into the training loop while dynamically balancing resources between static and dynamic components.

In this paper, we propose Constrained Dynamic Gaussian Splatting (CDGS), a framework that reformulates dynamic scene reconstruction as a budget-constrained optimization problem, as illustrated in Fig. 1. Departing from the conventional paradigm of uncontrolled growth, CDGS treats the Gaussian count as a strict budget. By optimizing the spatio-temporal distribution within this user-defined limit, it not only ensures precise controllability but also pushes the Pareto frontier of rate-distortion performance. Our approach is built upon three key innovations. First, to enforce the target capacity, we introduce a differentiable budget controller. This mechanism is driven by a differentiable budget loss guided by a multi-modal unified importance score, which fuses geometric stability, kinematic significance, and perceptual impact. This ensures that visually critical dynamic details are preserved even under tight budgets.

Second, to ensure robust adaptability across varying scene dynamics, we introduce an adaptive dynamic-static allocation method. Instead of relying on heuristic ratios, we leverage distribution analysis to autonomously identify the natural boundary between static and dynamic components, ensuring that the limited Gaussian budget is invested where it contributes most to the rendering quality. Third, we implement a three-phase training strategy to seamlessly integrate these



Fig. 1: **Left:** Our CDGS leverages differentiable budget control for precise Gaussian number regulation, achieving adaptive static-dynamic allocation across varying target numbers and optimal rendering quality. **Middle:** Visual comparison with state-of-the-art methods, highlighting advantages in visual quality, model size, and Gaussian count controllability (second row: actual/target counts). **Right:** Superior rate-distortion performance and precise Gaussian number control of our approach, outperforming all prior works (e.g. 4DGS [21], STGS [22], Ex4DGS [23]).

constraints, ensuring precise adherence to the target count (error < 2%). Finally, to minimize storage footprint, a dual-mode hybrid compression strategy is tailored specifically for the decomposed static and dynamic streams.

Collectively, these innovations enable CDGS to deliver controllable, compact, and high-quality FVV representations tailored to arbitrary hardware specifications. Experimental results demonstrate a 3x model size reduction compared to state-of-the-art methods while maintaining comparable quality. In summary, our contributions are as follows:

- We reinterpret dynamic Gaussian splatting as a budget-constrained optimization problem, enabling controllable model complexity and predictable capacity.
- We introduce a differentiable budget controller guided by a unified importance score, together with an autonomous adaptive static-dynamic allocation strategy that optimizes Gaussian distribution under a fixed budget.
- We design a budget-consistent three-phase training scheme and a dual-mode hybrid compression pipeline that jointly enforce strict budget adherence while minimizing spatio-temporal redundancy.
- Extensive experiments across multiple datasets show that CDGS consistently outperforms existing dynamic scene reconstruction methods, achieving superior rate-distortion performance and precise Gaussian count control.

## II. RELATED WORK

### A. Novel View Synthesis for Static Scenes

NeRF [9] revolutionized novel view synthesis by parameterizing continuous radiance fields with Multi-Layer Perceptrons, yet its reliance on expensive ray marching imposes prohibitive computational costs. To mitigate this, subsequent works [10]–[15], [27]–[31] adopted structured representations such as voxel grids, octrees, and hash tables to accelerate the query process. While these hybrid approaches significantly improve training and rendering efficiency, they fundamentally remain

bound by the ray-marching paradigm, where the requisite point-wise sampling along each ray continues to limit the optimal balance between high-frequency detail capture and computational throughput.

Marking a paradigm shift from implicit ray marching, 3DGS [24] and its variants [32]–[41] leverage explicit anisotropic Gaussians and tile-based GPU rasterization to achieve superior visual quality in real-time. However, this explicit nature introduces new challenges: the adaptive density control strategy allows the number of primitives to grow unboundedly, resulting in high and variable memory usage that often exceeds consumer-grade hardware capacities. This uncontrolled model complexity and unstable convergence pattern severely hinder the deployment of 3DGS under strict computational or memory budgets, necessitating more robust control mechanisms.

### B. Novel View Synthesis for Dynamic Scenes

Extending view synthesis to dynamic environments requires addressing complex motion and temporal redundancy. Early approaches adapted the NeRF framework, either by introducing deformation fields [16]–[20], [42]–[45] to map time-variant observations to a canonical space, or by adopting 4D spatio-temporal representations [46]–[54] like 4D grids. While deformation-based methods struggle with large topological changes, 4D spatio-temporal representations often incur significant memory costs and inherit the slow rendering speeds of implicit methods.

With the advent of 3DGS, research has shifted towards explicit dynamic modeling, generally falling into two streams. The first stream [21]–[23], [25], [55]–[62] utilizes unified 4D primitives or time-dependent attributes for continuous interpolation, while the second [63]–[68] employs frame-by-frame tracking or streaming updates to handle topological changes. Notably, methods like Ex4DGS [23] and DeGauss [69] further decompose scenes into static and dynamic components. Despite these advances, current dynamic 3DGS methods typically

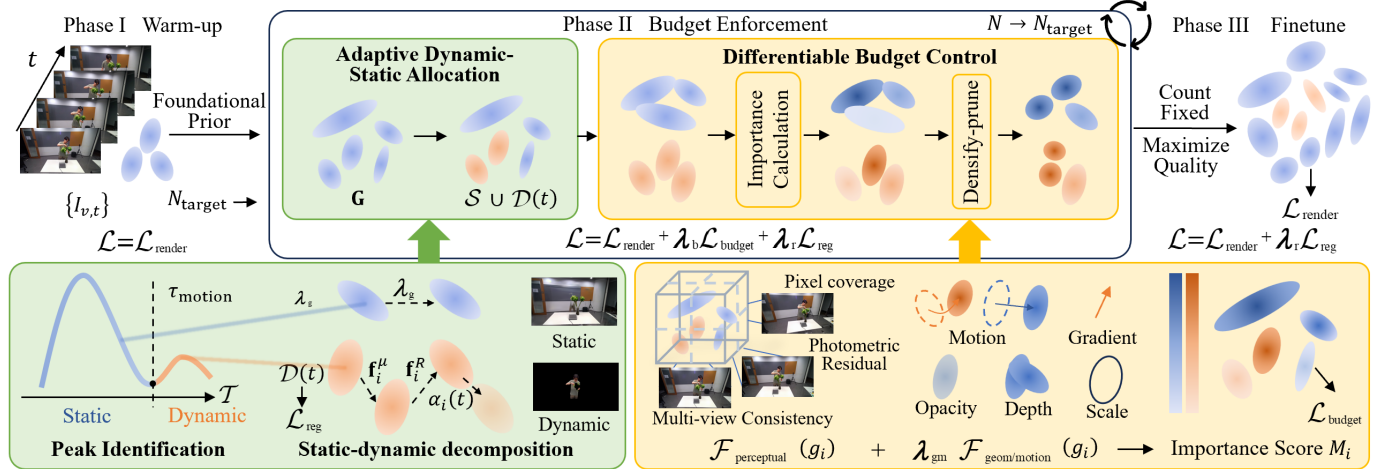


Fig. 2: Overview of the proposed CDGS framework. **(Top)** Three-Phase Pipeline: The training progresses from a Warm-up phase to establish foundational priors, through a Budget Enforcement phase where constraints are actively applied, to a final Fine-tuning phase that maximizes quality under the fixed count  $N_{\text{target}}$ . **(Bottom Left)** Adaptive Dynamic-Static Allocation: This module analyzes the distribution of motion magnitudes to identify a natural separation threshold  $\tau_{\text{motion}}$  via peak identification. It decomposes the scene into a Static set  $S$  and a Dynamic set  $D(t)$ . **(Bottom Right)** Differentiable Budget Control: This module regulates capacity by computing a Unified Importance Score  $M_i$ . It fuses Perceptual cues  $\mathcal{F}_{\text{perceptual}}$  and Geometric/Motion cues  $\mathcal{F}_{\text{geom/motion}}$ . The resulting score guides the differentiable budget loss  $\mathcal{L}_{\text{budget}}$  to precisely prune or densify Gaussians towards  $N_{\text{target}}$ .

rely on heuristic-driven densification, allowing the Gaussian count to grow arbitrarily. This unconstrained model complexity results in millions of redundant primitives, burdening storage and rendering efficiency without proportional visual gains.

### C. Gaussian Number Management

Deploying 3DGS on resource-constrained devices faces a fundamental conflict between limited hardware capacities and the standard optimization strategy, which minimizes error via unbounded densification. To alleviate storage pressure, recent compression-oriented methods [37], [70]–[72] propose techniques such as vector quantization or importance-based pruning. For instance, LightGaussian [37] prunes redundant Gaussians via significance scores, while C3DGS [71] utilizes codebook-based compression. However, these approaches predominantly operate in a train-then-prune or post-processing manner. They lack the mechanism to precisely align the model size with a predefined hardware budget during training. Consequently, removing primitives from a converged model often leads to suboptimal solutions and unpredictable quality degradation, as the remaining Gaussians are not jointly optimized to compensate for the information loss.

The most relevant work to ours is Taming 3DGS [26], which introduces a controlled growth schedule to maintain the Gaussian count near a target level. While effective for static objects, Taming 3DGS relies solely on geometric density and fails to address the complexities of dynamic scenarios, where temporal redundancy and motion blurring require more sophisticated importance assessment. To bridge this gap, we formulate dynamic reconstruction as a budget-constrained optimization problem. Distinct from passive compression, our method integrates the target count directly into the training

objective. By employing an adaptive static-dynamic allocation strategy and a differentiable budget controller, we ensure the model actively seeks the optimal configuration within the strict Gaussian budget, maximizing rendering fidelity while strictly adhering to the specified capacity limits.

## III. METHOD

We propose CDGS, a unified framework designed for high-fidelity dynamic 3D scene reconstruction under explicit resource constraints. Unlike prior methods prone to heuristic pruning or uncontrolled Gaussian growth, CDGS reformulates the reconstruction task as a budget-constrained optimization problem, enabling precise control over model capacity. As illustrated in Fig. 2, given multi-view video inputs and a target Gaussian count  $N_{\text{target}}$ , our pipeline is driven by a Differentiable Budget Controller (Sec. III-B). This module supervises densification and pruning based on a unified importance score that integrates geometric, motion, and perceptual cues. To maximize the utility of the fixed budget, an Adaptive Static-Dynamic Allocation module (Sec. III-C) redistributes the Gaussian budget across static and dynamic regions. The overall training follows a three-phase pipeline (Sec. III-D) to stabilize the representation, and employs a dual-mode hybrid compression scheme (Sec. III-E) to minimize storage and transmission overhead for efficient deployment.

### A. Problem Formulation

Given calibrated multi-view dynamic frames  $\{I_{v,t}\}$ , where  $v$  indexes views  $V$  and  $t$  indexes time, our goal is to reconstruct a compact spatio-temporal Gaussian scene representation  $G$  that enables real-time rendering under a fixed capacity budget

$N_{\text{target}}$ . Following 3D Gaussian Splatting [24], the scene is modeled as a set of anisotropic Gaussians  $\mathbf{G} = \{g_i\}$ :

$$g_i = \{\boldsymbol{\mu}_i, \mathbf{R}_i, \mathbf{s}_i, \alpha_i, \mathbf{f}_i\}, \quad (1)$$

where  $\boldsymbol{\mu}_i$  denotes the 3D center position. The geometric shape of each Gaussian is determined by a 3D covariance matrix  $\Sigma_i$ , which is decomposed into a rotation matrix  $\mathbf{R}_i$  and a scaling matrix  $\mathbf{s}_i$  to ensure positive semi-definiteness during optimization:

$$\Sigma_i = \mathbf{R}_i \mathbf{s}_i \mathbf{s}_i^T \mathbf{R}_i^T. \quad (2)$$

In terms of appearance, each Gaussian carries an opacity scalar  $\alpha_i \in [0, 1]$  and a set of spherical harmonics (SH) coefficients  $\mathbf{f}_i$  which encode view-dependent radiance. To render novel views, the 3D Gaussians are projected onto the 2D image plane using splatting techniques. The final color  $\hat{I}_{v,t}$  for a specific view  $v$  at time  $t$  is computed via differentiable  $\alpha$ -blending of the sorted Gaussians overlapping a pixel:

$$\hat{I}_{v,t} = \sum_{i \in |\mathbf{G}|} \text{color}_i \alpha'_i \prod_{j=1}^{i-1} (1 - \alpha'_j), \quad (3)$$

where  $\text{color}_i$  is the color decoded from  $\mathbf{f}_i$  based on the viewing direction, and  $\alpha'_i$  represents the effective opacity in 2D projection space. To drive the optimization of the Gaussian parameters, we minimize the discrepancy between the rendered image  $\hat{I}_{v,t}$  and the corresponding ground truth  $I_{v,t}$ . We supervise the reconstruction with a perceptual appearance loss:

$$\mathcal{L}_{\text{render}} = (1 - \lambda_{\text{ssim}}) \|\hat{I}_{v,t} - I_{v,t}\|_1 + \lambda_{\text{ssim}} \mathcal{L}_{\text{SSIM}}(\hat{I}_{v,t}, I_{v,t}), \quad (4)$$

Unlike prior dynamic Gaussian approaches that freely grow and prune Gaussians post-training, we explicitly constrain the representational capacity during optimization:

$$\min_{\mathbf{G}} \mathcal{L}_{\text{render}}(\mathbf{G}) \quad \text{s.t.} \quad |\mathbf{G}| \leq N_{\text{target}}. \quad (5)$$

This constraint directly governs runtime memory, rendering cost, and even streaming bitrate. Our objective is therefore not the unconstrained best reconstruction, but the best reconstruction achievable under a fixed Gaussian-number budget, which forms the foundation for our differentiable population control and adaptive allocation strategies described next.

### B. Differentiable Budget Control

Enforcing the hard constraint  $|\mathbf{G}| \leq N_{\text{target}}$  in Eq. 5 is challenging, since the Gaussian count is discrete and non-differentiable. We therefore design a differentiable population controller, as illustrated in Fig. 3, that (1) guides the contribution of Gaussians in rendering, (2) ranks them by importance for adaptive densification and pruning, and (3) penalizes deviations from the target capacity through a differentiable budget loss.

**Differentiable Counting.** Each Gaussian  $g_i$  is assigned a continuous activation variable  $c_i \in [0, 1]$ , implemented via a temperature-controlled hard-sigmoid gate with a learnable Gaussian importance score  $M_i$ . During rendering,  $c_i$  directly regulates the participation of the Gaussian, so Gaussians with

$c_i \approx 0$  contribute negligibly. The effective active count is estimated as a differentiable proxy:

$$N_p = \sum_i c_i. \quad (6)$$

To match the target capacity, we introduce a quadratic budget loss:

$$\mathcal{L}_{\text{budget}} = (N_p - N_{\text{target}})^2, \quad (7)$$

which drives  $N_p$  toward  $N_{\text{target}}$ . To enable differentiable optimization, the binary existence of each Gaussian is relaxed into a continuous activation  $c_i \in [0, 1]$ . This is achieved via a temperature-controlled Hard-Sigmoid function applied to the Gaussian's importance score  $M_i$ :

$$c_i = \text{clamp} \left( \frac{M_i - 0.5}{\tau_c} + 0.5, 0, 1 \right), \quad (8)$$

where  $\tau_c$  is the temperature parameter controlling the steepness of the gate, and  $M_i$  is the unified importance score detailed in the following part.

To physically enforce this selection within the rendering pipeline, we modulate the opacity of each Gaussian using this activation variable. The effective opacity  $\hat{\alpha}_i$  used in the splatting equation (Eq. 3) is redefined as:

$$\hat{\alpha}_i = c_i \cdot \alpha_i. \quad (9)$$

This modulation serves as a differentiable bridge: when  $c_i \rightarrow 0$ , the Gaussian becomes transparent and ceases to contribute to the image, physically aligning the soft deletion with the visual output. Crucially, this ensures that gradients from the rendering loss  $\mathcal{L}_{\text{render}}$  (Eq. 4) are back-propagated to the importance score  $M_i$  via  $c_i$ , establishing a cooperative optimization where perceptually critical Gaussians are protected from pruning.

The gate temperature is gradually annealed so that  $c_i$  approaches a binary mask. Specifically, the temperature  $\tau_c$  decays exponentially from an initial value  $\tau_{\text{init}}$  to a final value  $\tau_{\text{end}}$  during the budget enforcement phase. The decay schedule is formulated as:

$$\tau_c(k) = \tau_{\text{init}} \cdot \left( \frac{\tau_{\text{end}}}{\tau_{\text{init}}} \right)^{\frac{k - k_{\text{start}}}{k_{\text{end}} - k_{\text{start}}}}, \quad (10)$$

where  $k$  denotes the current iteration, and  $[k_{\text{start}}, k_{\text{end}}]$  represents the duration of the enforcement phase. In our experiments, we set  $\tau_{\text{init}} = 1.0$  and  $\tau_{\text{end}} = 0.01$  to ensure a smooth transition from soft gating to binary selection. Upon convergence, thresholding  $c_i$  yields an explicit active set with size  $\approx N_{\text{target}}$ . This converts the discrete constraint into a differentiable, Lagrangian-style penalty that is fully compatible with gradient-based optimization.

**Unified Importance Score.** To determine which Gaussians should survive under a strictly constrained budget, we require a metric that evaluates the contribution of each primitive to the final reconstruction. While previous pruning strategies like Taming 3DGS [26] focus solely on static geometric attributes, dynamic scenes introduce temporal redundancies and kinematic complexities that static metrics fail to capture. To address this, we define a unified importance score  $M_i$

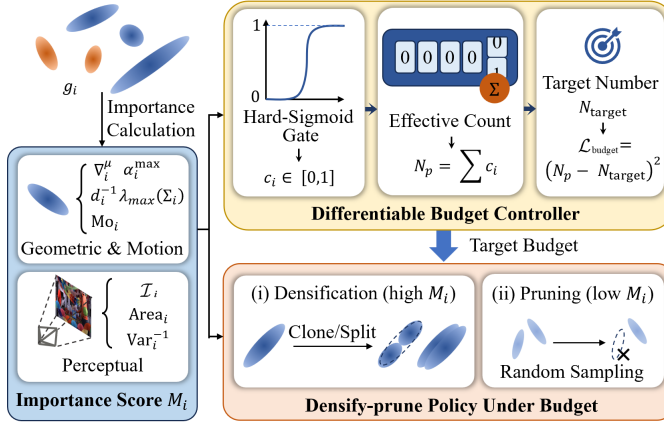


Fig. 3: Illustration of the Differentiable Budget Controller. The controller aggregates geometric, motion, and perceptual cues to compute a Unified Importance Score  $M_i$ . This score passes through a hard-sigmoid gate to estimate the effective Gaussian count  $N_p$ , which is strictly regulated towards the target  $N_{\text{target}}$  via a quadratic budget loss  $\mathcal{L}_{\text{budget}}$ . Guided by this budget constraint, the closed-loop policy performs densification on high-importance Gaussians and pruning on low-importance ones to dynamically optimize capacity.

that fuses geometric stability, kinematic significance, and perceptual impact:

$$M_i = \mathcal{N}(\lambda_{gm} \cdot \mathcal{F}_{\text{geom/motion}}(g_i) + \mathcal{F}_{\text{perceptual}}(g_i)), \quad (11)$$

where  $\mathcal{N}(\cdot)$  denotes Min-Max normalization scaling values to  $[0, 1]$ , ensuring a balanced aggregation of multi-modal cues.

*Geometric and Motion Cues* ( $\mathcal{F}_{\text{geom/motion}}$ ). This module captures the structural and kinematic necessity of a Gaussian. To handle the complexity of dynamic scenes, we explicitly decompose the score into five key components:

$$\begin{aligned} \mathcal{F}_{\text{geom/motion}}(g_i) &= \mathbf{w}_1^T \cdot \mathcal{N} \left( \left[ \nabla_i^\mu, \alpha_i^{\max}, d_i^{-1}, \right. \right. \\ &\quad \left. \left. \lambda_{\max}(\Sigma_i), \text{Mo}_i \right] \right), \\ \nabla_i^\mu &= \|\nabla_\mu \mathcal{L}_i\|_2, \\ \alpha_i^{\max} &= \max_{t \in T_i} \alpha_i(t), \\ d_i^{-1} &= \frac{1}{|V|} \sum_v d_{i,v}^{-1}, \\ \text{Mo}_i &= \begin{cases} \|\mathcal{T}_i\|_2, & \text{if } g_i \in \mathcal{S} \\ \|\mathbf{f}_i^\mu\|_2 + \|\mathbf{f}_i^R\|_2, & \text{if } g_i \in \mathcal{D}(t) \end{cases} \end{aligned} \quad (12)$$

Here,  $\mathbf{w}_1$  serves as a weighting vector to balance the contribution of each term, where each component targets a specific geometric or kinematic property critical for high-fidelity reconstruction. Specifically, the Positional Gradient  $\nabla_i^\mu$  quantifies the sensitivity of the reconstruction loss with respect to the Gaussian's position, effectively identifying primitives located in structure-critical regions where spatial precision is paramount. To capture temporal transients, Peak Opacity  $\alpha_i^{\max}$  utilizes the maximum opacity over the temporal sequence

rather than the average, ensuring that fleeting structures are preserved rather than pruned due to low average visibility. We further incorporate Proximity ( $d_i^{-1}$ ) via the inverse mean depth to explicitly prioritize foreground elements, as they occupy larger screen areas and demand higher rendering fidelity compared to distant background objects. To maintain background continuity, Spatial Extent  $\lambda_{\max}(\Sigma_i)$ , derived from the largest eigenvalue of the covariance matrix, safeguards large-scale Gaussians that cover extensive regions, preventing the formation of geometric holes. Finally, the Motion Magnitude  $\text{Mo}_i$  employs a piece-wise formulation adapted to our decomposition: for static Gaussians, it retains primitives necessary for correcting global translation, while for dynamic Gaussians, it prioritizes those exhibiting large displacements and rotations to protect high-frequency motion details that are otherwise difficult to recover.

*Perceptual Cues* ( $\mathcal{F}_{\text{perceptual}}$ ). To ensure visual fidelity, this component quantifies the rendering degradation caused by removing a Gaussian, aggregated across training views  $V$ :

$$\begin{aligned} \mathcal{F}_{\text{perceptual}}(g_i) &= \mathbf{w}_2^T \cdot \mathcal{N} \left( \left[ \mathcal{I}_i, \text{Area}_i, \text{Var}_i^{-1} \right] \right), \\ \mathcal{I}_i &= \sum_{v \in V} \|\mathcal{I}_v - \mathcal{I}_v^{\setminus \{i\}}\|_1, \\ \text{Area}_i &= \sum_{v \in V} \text{Area}_{i,v}, \\ \text{Var}_i^{-1} &= \text{Var}_{v \in V} (c_{i,v})^{-1}. \end{aligned} \quad (13)$$

Here,  $\mathbf{w}_2$  denotes the weighting vector that balances the contribution of each perceptual metric. Specifically, the Photometric Residual  $\mathcal{I}_i$  directly quantifies the rendering degradation by aggregating the pixel-wise L1 error introduced to the rendered image when the Gaussian  $g_i$  is excluded. To evaluate visual impact, Pixel Coverage  $\text{Area}_i$  accumulates the projected screen area of the Gaussian across views, where larger footprints imply a greater contribution to the final appearance. Finally, Multi-view Consistency  $\text{Var}_i^{-1}$  utilizes the inverse variance of the Gaussian's contribution across views to prioritize view-consistent primitives, effectively acting as a filter to suppress view-dependent noise or artifacts that would otherwise be visually distracting.

**Densify-prune Policy Under Budget.** Guided by the importance score  $M_i$  and regulated by a predefined budget, our method performs densification and pruning in a unified framework. The global target  $N_{\text{target}}$  is dynamically decomposed into a per-iteration sub-target via a quadratic schedule, as proposed in [26], throughout the training process. This decomposition guides a closed-loop controller for population evolution: (i) *densification*: Gaussians with high  $M_i$  are cloned or split with higher probability, ensuring computational resources are allocated to perceptually salient regions by injecting detail where needed; (ii) *pruning*: Gaussians with low  $M_i$  are targeted for removal via a random sampling strategy, gradually eliminating redundant or visually insignificant ones while preserving perceptually critical structures.

This closed-loop controller dynamically reallocates the Gaussian budget to the most informative spatial and temporal

regions while keeping the overall count near  $N_{\text{target}}$ . Unlike heuristic grow-and-prune pipelines [23], [25], our differentiable control embeds capacity regulation directly into optimization, enabling stable training and precise runtime control over model complexity.

### C. Adaptive Dynamic-Static Allocation

Dynamic scenes are rarely uniformly active: while the majority of regions often remain largely static or undergo rigid, regular motion, significant non-rigid deformations are typically confined to specific objects within limited temporal spans. Consequently, uniformly distributing Gaussians across space and time results in a substantial waste of representational capacity. To address this and fully utilize the fixed Gaussian budget  $N_{\text{target}}$ , we introduce an Adaptive Static-Dynamic Allocation strategy designed to maximize efficiency under strict constraints.

This mechanism decomposes the scene into a static field and a dynamic field, parameterizing their temporal behaviors separately. We represent the full Gaussian set  $\mathbf{G}$  as the union of two disjoint subsets,

$$\mathbf{G} = \mathcal{S} \cup \mathcal{D}(t), \quad \mathcal{S} \cap \mathcal{D}(t) = \emptyset. \quad (14)$$

Here,  $\mathcal{S}$  comprises time-invariant Gaussians responsible for the static objects, while  $\mathcal{D}(t)$  contains time-varying Gaussians dedicated to handling motion and deformation. Instead of relying on pre-labeled masks, heuristic priors, or fixed static-dynamic ratios, we propose to infer this decomposition automatically in a fully data-driven manner.

Our core insight is to frame the separation task as identifying a natural boundary within the distribution of motion magnitudes. We first assign each Gaussian  $g_i$  a translational attribute  $\mathcal{T}_i$  to characterize its motion intensity. After an initial warm-up phase, we analyze the intrinsic distribution properties of  $\{\mathcal{T}_i\}$  to determine the optimal separation. Formally, we construct a distribution histogram of motion magnitudes using  $B$  bins and apply smoothing to suppress noise. Let  $\mathbf{H}_{\mathcal{T}}$  denote the smoothed histogram and  $\mathcal{P}_{\mathcal{T}}$  be the set of identified peaks:

$$\begin{aligned} \mathbf{H}_{\mathcal{T}} &= \text{smooth}(\text{hist}(\mathcal{T}_i, B)), \\ \mathcal{P}_{\mathcal{T}} &= \{p \in B \mid \mathbf{H}_{\mathcal{T}}(p) > \mathbf{H}_{\mathcal{T}}(p \pm 1)\}. \end{aligned} \quad (15)$$

This smoothed histogram typically exhibits a bimodal distribution, corresponding to the distinct populations of static and dynamic elements. From the set of peaks  $\mathcal{P}_{\mathcal{T}}$ , we identify the two most significant modes, denoted as  $p_s$  and  $p_d$ , representing the centroids of the static and dynamic clusters, respectively. To achieve a clean separation, we locate the valley between these two peaks, which signifies the boundary where the probability density of mixed states is lowest:

$$\begin{aligned} \{p_s, p_d\} &= \underset{\{p_1, p_2\} \subseteq \mathcal{P}_{\mathcal{T}}, p_1 \neq p_2}{\text{argmax}} (\mathbf{H}_{\mathcal{T}}(p_1) + \mathbf{H}_{\mathcal{T}}(p_2)), \\ \tau_s &= \underset{x \in \{p_s, p_d\}}{\text{argmin}} \mathbf{H}_{\mathcal{T}}(x). \end{aligned} \quad (16)$$

Here,  $\tau_s$  represents the initial separation threshold in the histogram domain. To ensure robustness against binning ar-

tifacts and outliers, we map this threshold back to the data domain by calculating an adaptive percentile  $\alpha_{\mathcal{T}}$ :

$$\alpha_{\mathcal{T}} = \frac{|\{\mathcal{T}_i \mid \mathcal{T}_i < \tau_s\}|}{|\mathcal{T}_i|}, \quad \tau_{\text{motion}} = \text{quantile}(\{\mathcal{T}_i\}, \alpha_{\mathcal{T}}). \quad (17)$$

The resulting  $\tau_{\text{motion}}$  serves as the final, adaptive threshold. This formulation enables our method to automatically adapt to varying scene dynamics, providing an optimal separation that emerges naturally from the data distribution without manual parameter tuning.

Based on this classification, we apply distinct parameterization strategies to ensure model compactness. The static Gaussians  $\mathcal{S}$  maintain time-invariant attributes (position, rotation, scale, color) throughout the sequence, incorporating lightweight, per-frame global transforms  $\mathcal{T}_i$  to accommodate minor camera misalignments or lighting changes without redundant per-Gaussian updates. Conversely, the dynamic Gaussians  $\mathcal{D}(t)$  are equipped with explicit temporal parameters to capture complex motions. Each  $g_i \in \mathcal{D}(t)$  carries a position vector  $\mathbf{f}_i^{\mu}$  and a rotation vector  $\mathbf{f}_i^R$  (interpolated at time  $t$  to determine the instantaneous state), alongside a scale  $s_i$ , spherical harmonics coefficients  $\mathbf{f}_i$ , and a learnable activation window  $[t_i^s, t_i^e]$ . To enforce temporal sparsity, the opacity  $\alpha_i(t)$  is designed to decay smoothly outside this interval, ensuring that a dynamic Gaussian only consumes computational resources when it effectively contributes to the rendering.

Ultimately, this derived static-dynamic decomposition serves as a critical prior for our resource management. We allocate the Gaussian budget proportionally: regions identified as  $\mathcal{D}(t)$  or frames exhibiting higher dynamic activity receive a denser representation budget, while static regions  $\mathcal{S}$  retain compact but stable coverage. This decomposition directly guides the Differentiable Controller (Sec. III-B), instructing it on where Gaussian capacity should be invested across space and time. Together, this joint mechanism effectively balances reconstruction fidelity and storage efficiency, achieving high-quality dynamic rendering under strict model capacity constraints.

### D. Training Strategy

Training our constrained dynamic Gaussian model involves jointly optimizing scene appearance, differentiable budget control, and adaptive allocation in a stable and progressive manner. We adopt a three-phase training strategy designed to (i) obtain a reliable initialization, (ii) introduce differentiable population control, and (iii) stabilize optimization while enforcing the capacity constraint.

**Phase I: Warm-up and Initialization.** We begin with a short warm-up stage that initializes the representation without budget constraints. We utilize static Gaussians equipped with per-frame global transforms, allowing the model to roughly cover the scene geometry and rigid motion using only the rendering loss  $\mathcal{L}_{\text{render}}$  (Eq. 4). These pre-trained Gaussians serve as a foundational prior, providing reliable geometric and kinematic guidance for the subsequent modules.

**Phase II: Differentiable Budget Enforcement.** After warm-up, we activate the population controller (Sec. III-B)

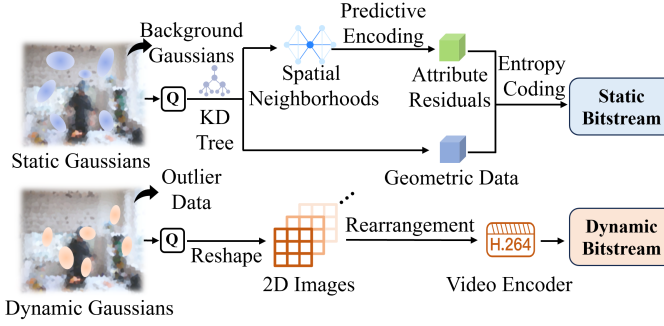


Fig. 4: Illustration of our dual-mode hybrid compression strategy, which separates outliers from both static and dynamic Gaussian data, then applies distinct compression approaches.

and introduce the budget loss  $\mathcal{L}_{\text{budget}}$  and regularization  $\mathcal{L}_{\text{reg}}$ . The total loss is formulated as:

$$\mathcal{L} = \mathcal{L}_{\text{render}} + \lambda_b \mathcal{L}_{\text{budget}} + \lambda_r \mathcal{L}_{\text{reg}} \quad (18)$$

where  $\lambda_b$  and  $\lambda_r$  control the strength of the budget penalty and regularization, respectively. Crucially, the Adaptive Dynamic-Static Allocation (Sec. III-C) is performed periodically alongside the densification and pruning operations. At each interval, the budget is dynamically redistributed between static and dynamic sets based on the updated motion priors. Simultaneously, discrete pruning is triggered for Gaussians with low opacity or near-zero mask values ( $c_i \approx 0$ ), while the gate temperature is annealed to gradually enforce a binary selection.

**Phase III: Stabilization and Fine-tuning.** Once the effective count  $N_p$  converges near  $N_{\text{target}}$ , we enter a stabilization phase. The soft masks  $c_i$  are explicitly binarized, and redundant Gaussians (where  $c_i = 0$ ) are permanently culled to strictly satisfy the budget constraint. The remaining compact set is then fine-tuned solely with  $\mathcal{L}_{\text{render}}$  and  $\mathcal{L}_{\text{reg}}$  to recover any detail loss caused by the masking process and to ensure temporal smoothness.

#### E. Dual-Mode Hybrid Compression

To further reduce storage and transmission cost under the fixed Gaussian budget, we adopt a dual-mode hybrid compression strategy tailored to the static and dynamic components introduced in Sec. III-C.

**Static Compression.** For static Gaussians, we observe that outliers far from the scene center significantly degrade the post-compression quality. This is because these distant points excessively expand the coordinate bounding box. Under uniform quantization, an expanded range forces a larger quantization step size, which drastically reduces the precision allocated to the densely populated foreground regions. To mitigate this, we first compute the mean  $\mu_d$  and standard deviation  $\sigma_d$  of all Gaussian distances to the scene center and separate background Gaussians using a threshold of  $\mu_d + 3\sigma_d$ . For the remaining foreground, after attribute quantization, we employ a KD-tree to spatially reorder points, ensuring local continuity. Leveraging these spatial neighborhoods, we apply predictive encoding to residuals to reduce entropy. Finally, geometric data

and attribute residuals undergo entropy encoding to complete the compression.

**Dynamic Compression.** For dynamic Gaussians, we first conduct a statistical analysis of the data distribution across channels, observing that: (1) distributions within the same attribute are highly similar across channels; and (2) each attribute is generally concentrated but contains significant outliers. Based on these findings, we design a dedicated compression pipeline. First, we separate top 5% of outlier data to narrow the value range and improve concentration. Next, we reshape each quantized attribute of the dynamic Gaussians into a 2D image format and rearrange them by grouping identical attributes together. These organized video sequences are then encoded using an H.264 encoder (based on the x264 library). To ensure high fidelity and temporal consistency, the encoder is configured with the YUV 4:4:4 color space, the “medium” preset, and a constant Quantization Parameter of 20. Furthermore, we restrict the encoding to I- and P-frames (disabling B-frames) with 3 reference frames to optimize for decoding efficiency.

## IV. EXPERIMENTS

### A. Configurations

**Datasets.** We evaluate our method on three challenging real-world datasets representing different dynamic characteristics. First, the N3DV dataset [50] provides 6 scenes with complex non-rigid deformations, captured by 18-21 cameras at  $2704 \times 2028$  resolution and 30 FPS. Second, the Technicolor dataset [74] offers studio-quality scenes recorded by a 16-camera rig at  $2048 \times 1088$ , featuring rich textures and lighting effects. Third, the MeetRoom dataset [75] captures long-duration human activities in an indoor setting using 14 cameras at  $1280 \times 720$  and 30 FPS. Consistent with prior works [23], [64], we employ a standard leave-one-out strategy. For the N3DV and Meetroom datasets, the first camera view is held out for testing. In contrast, for the Technicolor dataset, we reserve the camera positioned at the intersection of the second row and second column for evaluation. All remaining views serve as the training set.

**Implementation.** The experiments were conducted on hardware with an Intel(R) Xeon(R) W-2245 CPU @ 3.90 GHz and an RTX 3090 graphics card. For each sequence, our three-phase training strategy consists of 500, 29500, and 10000 iterations, respectively, with Gaussian densification and pruning performed every 500 steps during the second phase.  $\lambda_{\text{ssim}} = 0.2$ ,  $\lambda_b = 1 \times 10^{-7}$ ,  $\lambda_r = 1 \times 10^{-4}$  and  $\lambda_{\text{gm}} = 2$  were set for all sequences. In the compression phase, 16-bit quantization was used for  $\mu$ ,  $\mathcal{T}$  and  $f_\mu$ , while 8-bit quantization was applied to all other attributes.

**Metrics.** To assess the modeling and control capabilities of our method across experimental datasets, we adopt Peak Signal-to-Noise Ratio (PSNR) and Structural Similarity Index (SSIM) [76] as quality metrics, along with model size measured in megabytes for the entire sequence. For comprehensive rate-distortion performance analysis, we apply Bjontegaard Delta PSNR (BD-PSNR) [77]. Rendering efficiency is gauged by frames per second (FPS). To validate our method’s capacity

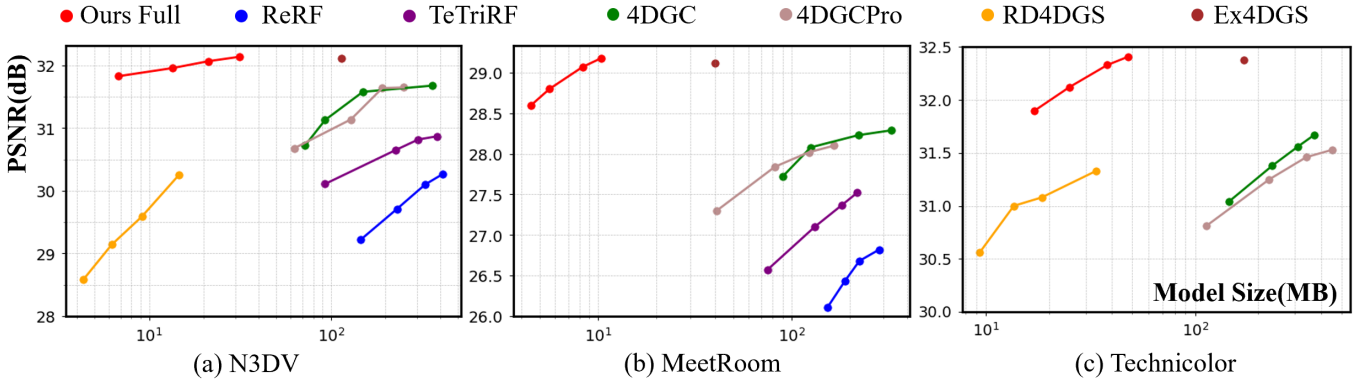


Fig. 5: Rate-distortion curves on different datasets, illustrating the superiority of our method over ReRF [17], TeTriRF [73], 4DGC [65], 4DGCP [66], RD4DGS [60] and Ex4DGS [23].

TABLE I: Quantitative comparison on the N3DV [50] dataset. The PSNR, SSIM, and rendering speed are averaged over all 300 frames for each scene. The reported model size is the total for the entire sequence. Ours-1 and Ours-s are obtained by setting the target Gaussian numbers to 300,000 and 100,000, respectively. **Best** and second best results are highlighted.

Method	PSNR↑ (dB)	SSIM↑	Size↓ (MB)	Render↑ (FPS)	Controll- able
K-Planes [48]	29.91	0.920	300	0.15	✗
ReRF [17]	29.71	0.918	231	2.0	✗
TeTriRF [73]	30.65	0.931	227	2.7	✗
StreamRF [75]	30.61	0.930	2280	8.3	✗
3DGStream [64]	31.54	0.942	2430	<b>215</b>	✗
4DGC [65]	31.58	0.943	150	168	✗
4DGCP [66]	31.64	0.943	192	170	✗
4DGaussians [25]	31.15	0.939	34	147	✗
4DG [21]	32.01	0.944	6270	72	✗
STGS [22]	32.05	0.944	200	107	✗
RD4DGS [60]	29.66	0.917	11.1	100.9	✗
Swift4D [62]	31.79	0.944	30	128	✗
GIFStream [61]	31.75	0.938	<u>10</u>	95	✗
Ex4DGS [23]	<u>32.11</u>	<u>0.945</u>	115	128	✗
Ours-1	<b>32.14</b>	<b>0.946</b>	31.5	149	✓
Ours-s	31.83	0.944	<b>6.8</b>	<u>186</u>	✓

TABLE II: Validation of our precise control capability over the total number of Gaussians. We report the average PSNR on the coffee\_martini sequence, the number of static/dynamic/overall Gaussians, and the error ratio of Gaussian number.

Method	Target	PSNR	Static	Dynamic	Overall	Ratio
Ex4DGS [23]	-	28.79	292.2k	47.7k	339.9k	-
Ours	100k	28.53	72.4k	27.6k	99.9k	0.1%
	200k	28.68	156.8k	41.0k	197.8k	1.1%
	300k	28.81	244.4k	51.4k	295.8k	1.4%
	400k	28.95	316.4k	81.2k	397.6k	0.6%

for Gaussian count control, we further report the number of Gaussians and the error ratio relative to the target.

### B. Comparison

**Quantitative Comparisons.** To validate the effectiveness of our method, we compare it against several state-of-the-art approaches, in particular those based on 3DGS, including

TABLE III: Quantitative comparison on the MeetRoom dataset [75] and Technicolor dataset [74].

Dataset	Method	PSNR↑ (dB)	SSIM↑	Size↓ (MB)	Render↑ (FPS)
MeetRoom Dataset [75]	ReRF [17]	26.43	0.911	189	2.9
	TeTriRF [73]	27.37	0.917	183	3.8
	StreamRF [75]	26.71	0.913	2469	10
	3DGStream [64]	28.03	0.921	2430	<b>288</b>
	4DGC [65]	28.08	0.922	126	213
	4DGCP [66]	28.02	0.921	123	<u>222</u>
	STGS [22]	29.01	0.929	15.2	159
	Ex4DGS [23]	29.12	<u>0.930</u>	40.2	148
Technicolor [74]	Ours-1	<b>29.18</b>	<b>0.931</b>	<u>10.4</u>	165
	Ours-s	28.60	0.927	<b>4.5</b>	215
	4DGC [65]	31.56	0.939	310	<u>139</u>
	4DGCP [66]	31.53	0.939	453	133
	STGS [22]	31.96	<u>0.941</u>	58.7	113
	RD4DGS [60]	31.33	0.938	<u>33.6</u>	123
	Ex4DGS [23]	<u>32.38</u>	<b>0.942</b>	170.3	100
	Ours-1	<b>32.41</b>	<b>0.942</b>	48.0	125
	Ours-s	31.90	0.940	<b>17.1</b>	<b>144</b>

3DGStream [64], 4DGC [65], 4DGCP [66], 4DGaussians [25], 4DGS [21], STGS [22], RD4DGS [60], Swift4D [62], GIFStream [61] and Ex4DGS [23]. We present two variants of our method, **Ours-1** and **Ours-s**, obtained by setting different target Gaussian numbers to demonstrate its scalability. Tab. I shows the detailed quantitative results on the N3DV dataset. As observed from the table, our method achieves the optimal rate-distortion performance. Specifically, 4DGS, STGS and Ex4DGS achieve reconstruction quality comparable to that of our method, but they typically require hundreds to thousands of MB in model size to enable dynamic scene reconstruction, whereas ours only requires **31.5 MB**. 4DGaussians, RD4DGS, Swift4D and GIFStream achieve a model size similar to that of our method, but results in varying degrees of PSNR degradation ranging from **0.08 dB** to **2.17 dB**. More importantly, we can achieve precise control over the total number of Gaussians. As shown in Tab. II, under different target total numbers of Gaussians, we maintain the error rate within **2%** and simultaneously achieve the optimal allocation of static and dynamic Gaussians.

We further validate the generality of our method on the

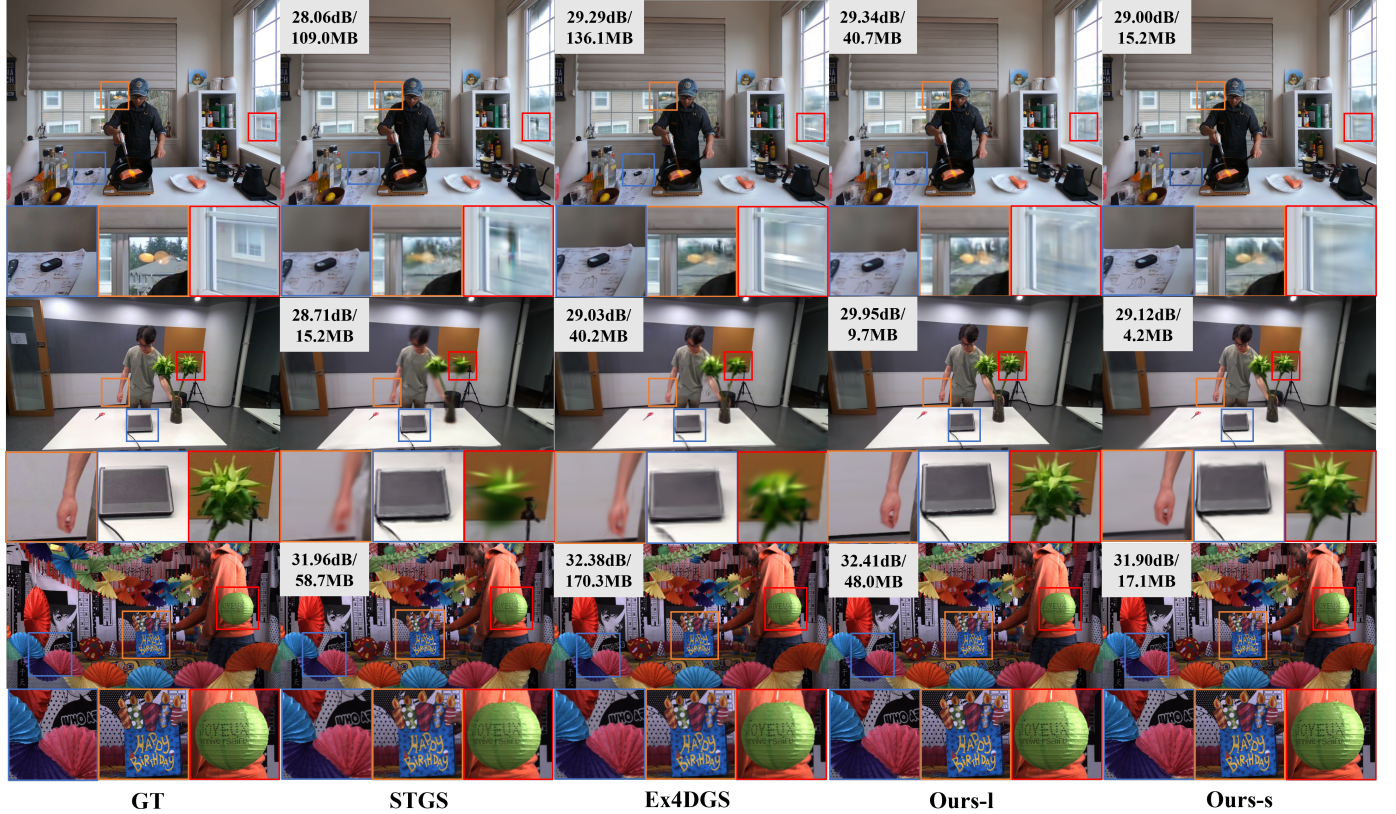


Fig. 6: Qualitative comparison of our CDGS against STGS [22] and Ex4DGS [23] on the N3DV [50], MeetRoom [75] and Technicolor [74] datasets, demonstrating the performance of CDGS under different target Gaussian numbers.

MeetRoom [75] and Technicolor [74] datasets. As summarized in Tab. III, our approach consistently outperforms a wide range of methods in PSNR, SSIM, and model size, corroborating its robustness across diverse scenes. What's more, we evaluate the rate-distortion performance against contemporary works, including ReRF [17], TeTriRF [73], 4DGC [65], 4DGCP [66], and RD4DGS [60]. As visualized in the RD curves of Fig. 5, our approach consistently pushes the Pareto frontier, outperforming variable-bitrate baselines across the spectrum. This superiority is also quantitatively corroborated by the BD-PSNR results in Tab. IV. Our method demonstrates the highest gains, with improvements over 4DGC of **1.90 dB** and **1.72 dB** on the N3DV and MeetRoom datasets, which is a substantial margin above all other comparisons.

Tab. V presents a comparison of computational efficiency between our CDGS and several dynamic scene reconstruction and compression methods. Our CDGS exhibits significantly improved computational efficiency: its training time is **1.0 hour**, compared to **1.2 hours** for Ex4DGS [23], owing to the increased interval of Gaussian expansion. Additionally, experimental results on the N3DV dataset demonstrate that our approach enables high-speed rendering, achieving a rate of **5.4 ms** per frame. For encoding and decoding, CDGS achieves times of **16 s** and **0.5 s** for 300 frames in total, respectively, outperforming all other methods by a significant margin. These results fully demonstrate that CDGS exhibits comprehensively fast performance across reconstruction, rendering, and encoding/decoding, confirming it as a highly efficient solution for

TABLE IV: The BD-PSNR(dB) results of our CDGS, ReRF [17], TeTriRF [73], 4DGCP [66] and RD4DGS [60] when compared with 4DGC [65] on different datasets.

Dataset	ReRF [17]	TeTriRF [73]	4DGCP [66]	RD4DGS [60]	Ours
N3DV [50]	-1.99	-1.12	0.08	1.33	<b>1.90</b>
MeetRoom [75]	-1.84	-0.86	-0.02	-	<b>1.72</b>

TABLE V: Complexity comparison of our method with dynamic scene reconstruction and compression methods.

Time	ReRF [17]	TeTriRF [73]	4DGC [65]	Ex4DGS [23]	Ours
Encode(s)	246	219	810	-	<b>16</b>
Decode(s)	18.3	16.8	28.2	-	<b>0.5</b>
Train(h)	>100	5.2	4.2	1.2	<b>1.0</b>
Render(ms)	497	372	5.6	7.8	<b>5.4</b>

constrained dynamic Gaussian splatting.

**Qualitative Comparisons.** As shown in Fig. 6, we qualitatively compare our method at different Gaussian number targets against STGS [22] and Ex4DGS [23] on the *flame\_salmon* sequence, the *trimming* sequence, and the *birthday* sequence. Our method delivers reconstruction quality comparable to these approaches while operating at a significantly lower model size. Compared to STGS, CDGS better preserves fine-grained details, such as the head, window, and desk in *flame\_salmon*, the fast-moving hands and intricate plants in *trimming*, as well as balloons, fans, and candles in *birthday*. Furthermore, our approach enables precise Gaus-

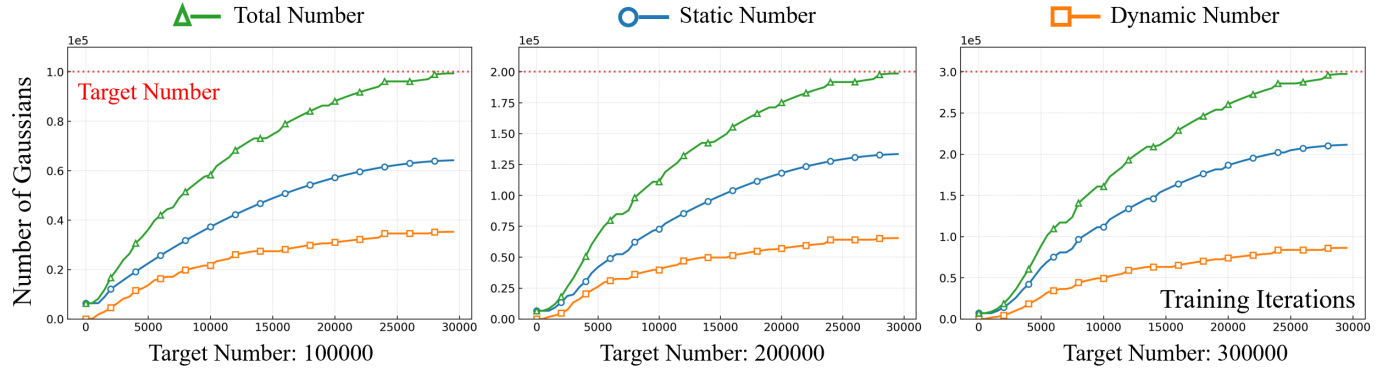


Fig. 7: Evolution of Gaussian counts under varying target budgets. The subplots correspond to target limits of  $1 \times 10^5$  (Left),  $2 \times 10^5$  (Middle), and  $3 \times 10^5$  (Right). The curves illustrate the growth trajectories of **Static**, **Dynamic**, and **Total** Gaussians. Under our constrained optimization framework, the total number steadily increases and converges precisely to the predefined Target Number.

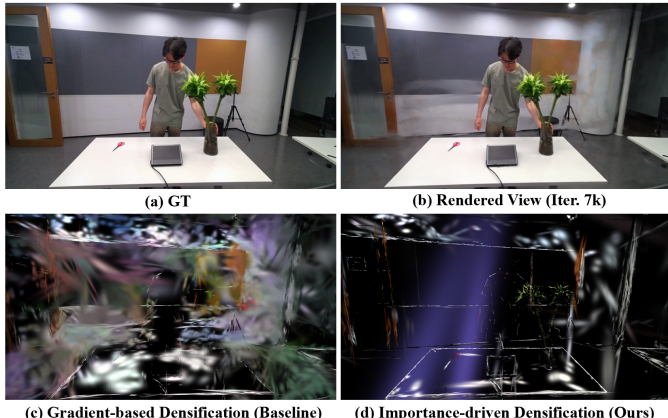


Fig. 8: Visualization of densification strategies at Iter. 7k. Unlike the gradient-based baseline (c) which generates excessive redundant primitives in the background, our importance-driven method (d) effectively suppresses irrelevant growth, concentrating Gaussians strictly on geometric and motion boundaries.

sian count control, consistently yielding optimal performance across varying total Gaussian numbers. For instance, in our lightweight variant (ours-s), reconstructing the *flame\_salmon* sequence requires only **10k** Gaussians, which is far fewer than the **35k** used by Ex4DGS. This underscores that CDGS not only accurately captures dynamic scene content and retains high-fidelity details in complex objects but also achieves a highly compact model size, all while realizing precise regulation of the Gaussian count.

### C. Evaluations

**Gaussian Number Constraint.** We conduct an ablation study to quantify the contribution of our proposed importance score and budget loss to Gaussian count control. As presented in Tab. VI, the unified importance score, which evaluates each Gaussian's actual rendering contribution, is more effective than relying on traditional training gradients. This superiority is visually explicated in Fig. 8. As shown in Fig. 8 (c),

TABLE VI: Evaluation results of our differentiable budget control and adaptive dynamic-static allocation.

	PSNR(dB)↑	Size(MB)↓	Ratio↓
w/o Importance score	31.91	31.2	1.6%
w/o $\mathcal{F}_{\text{geom/motion}}$	31.97	31.5	1.3%
w/o $\mathcal{F}_{\text{perceptual}}$	31.99	31.3	1.4%
$\lambda_{gm} = 1.5$	32.08	31.4	1.3%
$\lambda_{gm} = 2.5$	32.11	31.5	1.4%
w/o Budget loss	32.15	31.7	4.8%
w/o Adaptive allocation	31.96	33.2	1.3%
Ours full	32.14	31.5	1.3%

the gradient-based baseline struggles to distinguish between structural details and background noise, leading to blind densification in empty regions. Conversely, our method (Fig. 8 (d)) acts as a precise filter, concentrating the Gaussian budget solely on perceptually salient object boundaries. Ablating the entire importance score causes a significant performance drop of **0.23 dB**. The individual components of the score are also validated: removing the geometric/motion term ( $\mathcal{F}_{\text{geom/motion}}$ ) leads to a **0.17 dB** loss, while omitting the perceptual term ( $\mathcal{F}_{\text{perceptual}}$ ) results in a **0.15 dB** degradation. We further conduct a sensitivity analysis on the weighting coefficient  $\lambda_{gm}$ . Our experiments indicate that deviating from the default setting leads to varying degrees of quality degradation. This confirms that a balanced trade-off between geometric/motion stability and perceptual fidelity is essential for maximizing the utility of the limited Gaussian budget. Furthermore, the budget loss is proven critical for regulating the score distribution during training, ensuring the Gaussian count aligns with the target. Without it, the Gaussian count error increases by **3.5%**. This precise controllability is visually corroborated in Fig. 7. As observed, the total number of Gaussians monotonically increases and converges exactly to the preset limits without overshooting, demonstrating the stability and strictness of our budget enforcement enforcement strategy.

**Dynamic-Static Allocation.** Our adaptive allocation accurately determines the optimal static-dynamic ratio. As illustrated in Fig. 9, this approach achieves a more rational



Fig. 9: Visualization of our adaptive dynamic-static allocation strategy (**bottom**) against pre-defined ratio approach (**top**).

segmentation: it robustly assigns static elements like walls, stools, and cabinets to the static model, while accurately capturing motion regions such as hands and moving dogs. This optimized allocation directly contributes to superior overall rendering quality. The necessity of this module is quantitatively confirmed in Tab. VI, whose removal leads to a **-0.18 dB** drop in PSNR and a slight model size increase of **1.7 MB**, underscoring its role in both compactness and fidelity.

**Three-phase Training Strategy.** We remove the first and third training stages, respectively, to isolate their contributions. As summarized in Tab. VII, the initialization stage provides a reliable Gaussian translation prior, which is critical for an accurate static-dynamic allocation. Ablating this stage leads to a sub-optimal allocation that hinders effective training, resulting in a performance drop of **1.24 dB**. Conversely, the fine-tuning stage further optimizes the Gaussian distributions and attributes after the target count is reached, leading to a notable refinement in reconstruction quality. Its removal causes a drop of **0.28 dB**, confirming its role in enhancing the final rendering fidelity.

**Compression Strategy.** To minimize data redundancy, we introduce a subsequent compression pipeline tailored for both static and dynamic Gaussians. As summarized in Tab. VII, this approach reduces the model size by **34.0 MB** for static and **32.8 MB** for dynamic Gaussians, with a marginal impact on rendering quality. Fig. 10 provides a comparative visualization of the storage distribution before and after compression. By contrasting the two states, it is evident that our dual-mode strategy not only significantly reduces the overall model size but also effectively restructures the data. Specifically, the 'After' distribution highlights the successful isolation of 'Background' static Gaussians and 'Outlier' dynamic data, ensuring that the majority of the storage budget is precisely allocated to the perceptually critical foreground and motion details, thereby validating our separation strategy. The regularization loss is so critical for refining the data distribution that its removal leads to a significant **0.75 dB** drop. Furthermore, we identify that separating outliers in both static and dynamic Gaussians is a

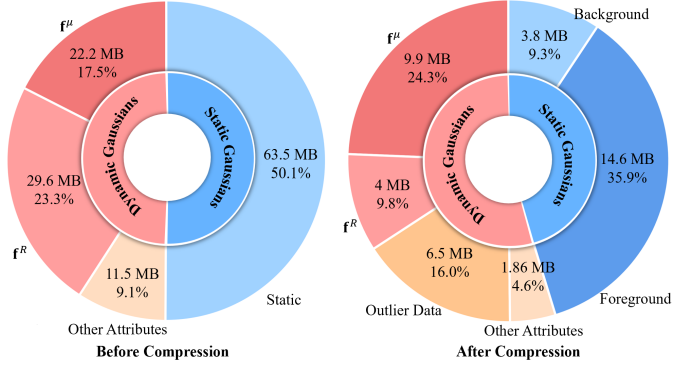


Fig. 10: Comparison of storage distribution before (**left**) and after (**right**) applying our dual-mode hybrid compression on the *flame\_salmon* sequence. The visualization highlights the significant reduction in model size and the explicit isolation of background and outlier components in the compressed representation.

TABLE VII: Evaluation results of our three-phase training strategy and dual-mode hybrid compression.

	PSNR(dB)↑	Size(MB)↓
w/o Initialization	30.90	31.8
w/o Fine-tuning	31.86	31.5
w/o Compression	32.21	98.3
w/o Static compression	32.19	65.5
w/o Dynamic compression	32.16	64.3
w/o Regularization loss	31.39	31.2
w/o Outlier separation	29.74	26.2
Ours full	32.14	31.5

critical prerequisite. Neglecting this step severely hampers the compression process, resulting in a substantial **2.4 dB** quality degradation.

## V. CONCLUSION

In this paper, we presented Constrained Dynamic Gaussian Splatting (CDGS), a framework that redefines dynamic scene reconstruction from an unconstrained fitting task to a budget-constrained optimization problem. Departing from heuristic train-then-prune paradigms, CDGS demonstrates that integrating hardware constraints directly into the training loop is essential for achieving optimal fidelity. Through our differentiable budget controller and adaptive static-dynamic allocation, underpinned by a progressive three-phase training strategy, we successfully resolved the complex spatio-temporal resource competition. Furthermore, coupled with a dual-mode hybrid compression scheme, CDGS ensures that limited capacity is intelligently invested in visually critical motion details while minimizing storage footprint. Extensive experiments validate that CDGS achieves superior rate-distortion performance, offering a robust and practical solution for deploying high-fidelity 4D immersive media on resource-constrained edge devices.

## REFERENCES

[1] Y. Wang, W. Wang, J. Ling, R. Xie, and L. Song, "Visibility-aware human mesh recovery via balancing dense correspondence and proba-

bility model," in *2024 IEEE International Conference on Multimedia and Expo Workshops (ICMEW)*, 2024, pp. 1–6.

[2] Y. Xia, X. Zhou, E. Vouga, Q. Huang, and G. Pavlakos, "Reconstructing humans with a biomechanically accurate skeleton," in *Proceedings of the IEEE/CVF Conference on Computer Vision and Pattern Recognition (CVPR)*, 2025.

[3] M. Yang, Z. Luo, M. Hu, M. Chen, and D. Wu, "A comparative measurement study of point cloud-based volumetric video codecs," *IEEE Transactions on Broadcasting*, vol. 69, no. 3, pp. 715–726, 2023.

[4] A. Akhtar, Z. Li, G. Van der Auwera, and J. Chen, "Dynamic point cloud interpolation," in *ICASSP 2022 - 2022 IEEE International Conference on Acoustics, Speech and Signal Processing (ICASSP)*, 2022, pp. 2574–2578.

[5] D. Graziosi, O. Nakagami, S. Kuma, A. Zaghetto, T. Suzuki, and A. Tabatabai, "An overview of ongoing point cloud compression standardization activities: Video-based (v-pcc) and geometry-based (g-pcc)," *APSIPA Transactions on Signal and Information Processing*, vol. 9, p. e13, 2020.

[6] S. Guo, J. Hu, K. Zhou, J. Wang, L. Song, R. Xie, and W. Zhang, "Real-time free viewpoint video synthesis system based on dibr and a depth estimation network," *IEEE Transactions on Multimedia*, vol. 26, pp. 6701–6716, 2024.

[7] J. M. Boyce, R. Doré, A. Dziembowski, J. Fleureau, J. Jung, B. Kroon, B. Salahieh, V. K. M. Vadakital, and L. Yu, "Mpeg immersive video coding standard," *Proceedings of the IEEE*, vol. 109, no. 9, pp. 1521–1536, 2021.

[8] Q. Hu, Q. He, H. Zhong, G. Lu, X. Zhang, G. Zhai, and Y. Wang, "Var-fvv: View-adaptive real-time interactive free-view video streaming with edge computing," *IEEE Journal on Selected Areas in Communications*, pp. 1–1, 2025.

[9] B. Mildenhall, P. P. Srinivasan, M. Tancik, J. T. Barron, R. Ramamoorthi, and R. Ng, "Nerf: Representing scenes as neural radiance fields for view synthesis," *Communications of the ACM*, vol. 65, no. 1, pp. 99–106, 2021.

[10] J. T. Barron, B. Mildenhall, M. Tancik, P. Hedman, R. Martin-Brualla, and P. P. Srinivasan, "Mip-nerf: A multiscale representation for anti-aliasing neural radiance fields," in *Proceedings of the IEEE/CVF international conference on computer vision*, 2021, pp. 5855–5864.

[11] J. T. Barron, B. Mildenhall, D. Verbin, P. P. Srinivasan, and P. Hedman, "Mip-nerf 360: Unbounded anti-aliased neural radiance fields," in *Proceedings of the IEEE/CVF conference on computer vision and pattern recognition*, 2022, pp. 5470–5479.

[12] A. Chen, Z. Xu, A. Geiger, J. Yu, and H. Su, "Tensorf: Tensorial radiance fields," in *European conference on computer vision*. Springer, 2022, pp. 333–350.

[13] T. Müller, A. Evans, C. Schied, and A. Keller, "Instant neural graphics primitives with a multiresolution hash encoding," *ACM transactions on graphics (TOG)*, vol. 41, no. 4, pp. 1–15, 2022.

[14] D. Duckworth, P. Hedman, C. Reiser, P. Zhizhin, J.-F. Thibert, M. Lučić, R. Szeliški, and J. T. Barron, "Smerf: Streamable memory efficient radiance fields for real-time large-scene exploration," *ACM Transactions on Graphics (TOG)*, vol. 43, no. 4, pp. 1–13, 2024.

[15] J. T. Barron, B. Mildenhall, D. Verbin, P. P. Srinivasan, and P. Hedman, "Zip-nerf: Anti-aliased grid-based neural radiance fields," in *Proceedings of the IEEE/CVF International Conference on Computer Vision*, 2023, pp. 19 697–19 705.

[16] L. Li, Z. Shen, Z. Wang, L. Shen, and P. Tan, "Streaming radiance fields for 3d video synthesis," *Advances in Neural Information Processing Systems*, vol. 35, pp. 13 485–13 498, 2022.

[17] L. Wang, Q. Hu, Q. He, Z. Wang, J. Yu, T. Tuytelaars, L. Xu, and M. Wu, "Neural residual radiance fields for streamably free-viewpoint videos," in *CVPR*, June 2023, pp. 76–87.

[18] L. Wang, K. Yao, C. Guo, Z. Zhang, Q. Hu, J. Yu, L. Xu, and M. Wu, "Videorf: Rendering dynamic radiance fields as 2d feature video streams," 2023.

[19] Z. Zheng, H. Zhong, Q. Hu, X. Zhang, L. Song, Y. Zhang, and Y. Wang, "Jointrf: End-to-end joint optimization for dynamic neural radiance field representation and compression," in *2024 IEEE International Conference on Image Processing (ICIP)*, 2024, pp. 3292–3298.

[20] —, "Hpc: Hierarchical progressive coding framework for volumetric video," in *ACM MM*, ser. MM '24. New York, NY, USA: Association for Computing Machinery, 2024, p. 7937–7946.

[21] Z. Yang, H. Yang, Z. Pan, and L. Zhang, "Real-time photorealistic dynamic scene representation and rendering with 4d gaussian splatting," in *ICLR*, 2024.

[22] Z. Li, Z. Chen, Z. Li, and Y. Xu, "Spacetime gaussian feature splatting for real-time dynamic view synthesis," in *CVPR*, June 2024, pp. 8508–8520.

[23] J. Lee, C. Won, H. Jung, I. Bae, and H.-G. Jeon, "Fully explicit dynamic gaussian splatting," in *Proceedings of the Neural Information Processing Systems*, 2024.

[24] B. Kerbl, G. Kopanas, T. Leimkühler, and G. Drettakis, "3d gaussian splatting for real-time radiance field rendering," *ACM Trans. Graph.*, vol. 42, no. 4, pp. 139–1, 2023.

[25] G. Wu, T. Yi, J. Fang, L. Xie, X. Zhang, W. Wei, W. Liu, Q. Tian, and X. Wang, "4d gaussian splatting for real-time dynamic scene rendering," in *CVPR*, June 2024, pp. 20 310–20 320.

[26] S. S. Mallick, R. Goel, B. Kerbl, M. Steinberger, F. V. Carrasco, and F. De La Torre, "Taming 3dgs: High-quality radiance fields with limited resources," in *SIGGRAPH Asia 2024 Conference Papers*, ser. SA '24. New York, NY, USA: Association for Computing Machinery, 2024.

[27] K. Zhang, G. Riegler, N. Snavely, and V. Koltun, "Nerf++: Analyzing and improving neural radiance fields," *arXiv preprint arXiv:2010.07492*, 2020.

[28] C. Sun, M. Sun, and H.-T. Chen, "Direct voxel grid optimization: Superfast convergence for radiance fields reconstruction," in *Proceedings of the IEEE/CVF conference on computer vision and pattern recognition*, 2022, pp. 5459–5469.

[29] A. Karnewar, T. Ritschel, O. Wang, and N. Mitra, "Relu fields: The little non-linearity that could," in *ACM SIGGRAPH 2022 conference proceedings*, 2022, pp. 1–9.

[30] M. Niemeyer, F. Manhardt, M.-J. Rakotosaona, M. Oechsle, D. Duckworth, R. Gosula, K. Tateno, J. Bates, D. Kaeser, and F. Tombari, "Radsplat: Radiance field-informed gaussian splatting for robust real-time rendering with 900+ fps," in *2025 International Conference on 3D Vision (3DV)*. IEEE, 2025, pp. 134–144.

[31] X. Zhang, S. Bi, K. Sunkavalli, H. Su, and Z. Xu, "Nerfusion: Fusing radiance fields for large-scale scene reconstruction," in *Proceedings of the IEEE/CVF conference on computer vision and pattern recognition*, 2022, pp. 5449–5458.

[32] D. Charatan, S. L. Li, A. Tagliasacchi, and V. Sitzmann, "pixelsplat: 3d gaussian splats from image pairs for scalable generalizable 3d reconstruction," in *Proceedings of the IEEE/CVF conference on computer vision and pattern recognition*, 2024, pp. 19 457–19 467.

[33] G. Feng, S. Chen, R. Fu, Z. Liao, Y. Wang, T. Liu, B. Hu, L. Xu, Z. Pei, H. Li et al., "Flashgs: Efficient 3d gaussian splatting for large-scale and high-resolution rendering," in *Proceedings of the Computer Vision and Pattern Recognition Conference*, 2025, pp. 26 652–26 662.

[34] Z. Gao, B. Planche, M. Zheng, A. Choudhuri, T. Chen, and Z. Wu, "6dgs: Enhanced direction-aware gaussian splatting for volumetric rendering," *arXiv preprint arXiv:2410.04974*, 2024.

[35] L. Höllerin, A. Božić, M. Zollhöfer, and M. Nießner, "3dgs-lm: Faster gaussian-splatting optimization with levenberg-marquardt," *arXiv preprint arXiv:2409.12892*, 2024.

[36] K. Navaneet, K. P. Meibodi, S. A. Koohpayegani, and H. Pirsiavash, "Compgs: Smaller and faster gaussian splatting with vector quantization," *ECCV*, 2024.

[37] Z. Fan, K. Wang, K. Wen, Z. Zhu, D. Xu, and Z. Wang, "Lightgaussian: Unbounded 3d gaussian compression with 15x reduction and 200+ fps," 2023.

[38] T. Lu, M. Yu, L. Xu, Y. Xiangli, L. Wang, D. Lin, and B. Dai, "Scaffoldgs: Structured 3d gaussians for view-adaptive rendering," in *CVPR*, 2024, pp. 20 654–20 664.

[39] Y. Wang, Z. Li, L. Guo, W. Yang, A. C. Kot, and B. Wen, "Contextgs: Compact 3d gaussian splatting with anchor level context model," *arXiv preprint arXiv:2405.20721*, 2024.

[40] H. Zhong, Z. Zheng, Q. Hu, Y. Tian, N. Cao, L. Xu, X. Zhang, Z. Cheng, L. Song, and W. Zhang, "4d-mode: Towards editable and scalable volumetric streaming via motion-decoupled 4d gaussian compression," 2025.

[41] Y. Gao, H. Zhong, T. Zhu, Z. Cheng, Q. Hu, and L. Song, "Aligngs: Aligning geometry and semantics for robust indoor reconstruction from sparse views," 2025.

[42] Y. Du, Y. Zhang, H.-X. Yu, J. B. Tenenbaum, and J. Wu, "Neural radiance flow for 4d view synthesis and video processing," in *2021 IEEE/CVF International Conference on Computer Vision (ICCV)*. IEEE Computer Society, 2021, pp. 14 304–14 314.

[43] K. Park, U. Sinha, J. T. Barron, S. Bouaziz, D. B. Goldman, S. M. Seitz, and R. Martin-Brualla, "Nerfies: Deformable neural radiance fields," in *Proceedings of the IEEE/CVF international conference on computer vision*, 2021, pp. 5865–5874.

[44] A. Pumarola, E. Corona, G. Pons-Moll, and F. Moreno-Noguer, “D-nerf: Neural radiance fields for dynamic scenes,” in *Proceedings of the IEEE/CVF conference on computer vision and pattern recognition*, 2021, pp. 10 318–10 327.

[45] L. Song, A. Chen, Z. Li, Z. Chen, L. Chen, J. Yuan, Y. Xu, and A. Geiger, “Nerfplayer: A streamable dynamic scene representation with decomposed neural radiance fields,” *IEEE Transactions on Visualization and Computer Graphics*, vol. 29, no. 5, pp. 2732–2742, 2023.

[46] A. Cao and J. Johnson, “Hexplane: A fast representation for dynamic scenes,” in *Proceedings of the IEEE/CVF Conference on Computer Vision and Pattern Recognition*, 2023, pp. 130–141.

[47] J. Fang, T. Yi, X. Wang, L. Xie, X. Zhang, W. Liu, M. Nießner, and Q. Tian, “Fast dynamic radiance fields with time-aware neural voxels,” in *SIGGRAPH Asia 2022 Conference Papers*, 2022, pp. 1–9.

[48] S. Fridovich-Keil, G. Meanti, F. R. Warburg, B. Recht, and A. Kanazawa, “K-planes: Explicit radiance fields in space, time, and appearance,” in *Proceedings of the IEEE/CVF Conference on Computer Vision and Pattern Recognition*, 2023, pp. 12 479–12 488.

[49] M. Işık, M. Rünz, M. Georgopoulos, T. Khakhulin, J. Starck, L. Agapito, and M. Nießner, “Humanrf: High-fidelity neural radiance fields for humans in motion,” *ACM Transactions on Graphics (TOG)*, vol. 42, no. 4, pp. 1–12, 2023.

[50] T. Li, M. Slavcheva, M. Zollhoefer, S. Green, C. Lassner, C. Kim, T. Schmidt, S. Lovegrove, M. Goesele, R. Newcombe *et al.*, “Neural 3d video synthesis from multi-view video,” in *Proceedings of the IEEE/CVF conference on computer vision and pattern recognition*, 2022, pp. 5521–5531.

[51] S. Park, M. Son, S. Jang, Y. C. Ahn, J.-Y. Kim, and N. Kang, “Temporal interpolation is all you need for dynamic neural radiance fields,” in *Proceedings of the IEEE/CVF conference on computer vision and pattern recognition*, 2023, pp. 4212–4221.

[52] R. Shao, Z. Zheng, H. Tu, B. Liu, H. Zhang, and Y. Liu, “Tensor4d: Efficient neural 4d decomposition for high-fidelity dynamic reconstruction and rendering,” in *Proceedings of the IEEE/CVF Conference on Computer Vision and Pattern Recognition*, 2023, pp. 16 632–16 642.

[53] F. Wang, S. Tan, X. Li, Z. Tian, Y. Song, and H. Liu, “Mixed neural voxels for fast multi-view video synthesis,” in *Proceedings of the IEEE/CVF International Conference on Computer Vision*, 2023, pp. 19 706–19 716.

[54] L. Wang, J. Zhang, X. Liu, F. Zhao, Y. Zhang, Y. Zhang, M. Wu, J. Yu, and L. Xu, “Fourier plenoctrees for dynamic radiance field rendering in real-time,” in *Proceedings of the IEEE/CVF Conference on Computer Vision and Pattern Recognition*, 2022, pp. 13 524–13 534.

[55] Z. Yang, X. Gao, W. Zhou, S. Jiao, Y. Zhang, and X. Jin, “Deformable 3d gaussians for high-fidelity monocular dynamic scene reconstruction,” *arXiv preprint arXiv:2309.13101*, 2023.

[56] J. Yan, R. Peng, L. Tang, and R. Wang, “4d gaussian splatting with scale-aware residual field and adaptive optimization for real-time rendering of temporally complex dynamic scenes,” in *ACM MM*, 2024, pp. 7871–7880.

[57] Y. Wang, P. Yang, Z. Xu, J. Sun, Z. Zhang, Y. Chen, H. Bao, S. Peng, and X. Zhou, “Freetimegs: Free gaussian primitives at anytime anywhere for dynamic scene reconstruction,” in *CVPR*, 2025.

[58] X. Zhang, Z. Liu, Y. Zhang, X. Ge, D. He, T. Xu, Y. Wang, Z. Lin, S. Yan, and J. Zhang, “Mega: Memory-efficient 4d gaussian splatting for dynamic scenes,” *arXiv preprint arXiv:2410.13613*, 2024.

[59] W. O. Cho, I. Cho, S. Kim, J. Bae, Y. Uh, and S. J. Kim, “4d scaffold gaussian splatting with dynamic-aware anchor growing for efficient and high-fidelity dynamic scene reconstruction,” 2025.

[60] H. Lee and K. Baek, “Temporal smoothness-aware rate-distortion optimized 4d gaussian splatting,” in *Advances in Neural Information Processing Systems*, 2025.

[61] H. Li, S. Li, X. Gao, A. Batuer, L. Yu, and Y. Liao, “Gifstream: 4d gaussian-based immersive video with feature stream,” 2025.

[62] J. Wu, R. Peng, Z. Wang, L. Xiao, L. Tang, J. Yan, K. Xiong, and R. Wang, “Swift4d: Adaptive divide-and-conquer gaussian splatting for compact and efficient reconstruction of dynamic scene,” *arXiv preprint arXiv:2503.12307*, 2025.

[63] J. Luiten, G. Kopanas, B. Leibe, and D. Ramanan, “Dynamic 3d gaussians: Tracking by persistent dynamic view synthesis,” in *3DV*, 2024.

[64] J. Sun, H. Jiao, G. Li, Z. Zhang, L. Zhao, and W. Xing, “3dgstream: On-the-fly training of 3d gaussians for efficient streaming of photo-realistic free-viewpoint videos,” in *CVPR*, June 2024, pp. 20 675–20 685.

[65] Q. Hu, Z. Zheng, H. Zhong, S. Fu, L. Song, X. Zhang, G. Zhai, and Y. Wang, “4dgc: Rate-aware 4d gaussian compression for efficient streamable free-viewpoint video,” in *Proceedings of the Computer Vision and Pattern Recognition Conference*, 2025, pp. 875–885.

[66] Z. Zheng, Z. Wu, H. Zhong, Y. Tian, N. Cao, L. Xu, J. Yao, X. Zhang, Q. Hu, and W. Zhang, “4dgcpro: Efficient hierarchical 4d gaussian compression for progressive volumetric video streaming,” *arXiv preprint arXiv:2509.17513*, 2025.

[67] Q. Gao, J. Meng, C. Wen, J. Chen, and J. Zhang, “Hicom: Hierarchical coherent motion for dynamic streamable scenes with 3d gaussian splatting,” in *Advances in Neural Information Processing Systems (NeurIPS)*, 2024.

[68] H. Zhong, Z. Wu, S. Fu, Z. Zheng, X. Jin, X. Zhang, L. Song, and Q. Hu, “Prismgs: Physically-grounded anti-aliasing for high-fidelity large-scale 3d gaussian splatting,” 2025.

[69] R. Wang, Q. Lohmeyer, M. Meboldt, and S. Tang, “Degauss: Dynamic-static decomposition with gaussian splatting for distractor-free 3d reconstruction,” 2025.

[70] S. Girish, K. Gupta, and A. Shrivastava, “Eagles: Efficient accelerated 3d gaussians with lightweight encodings,” 2024.

[71] J. C. Lee, D. Rho, X. Sun, J. H. Ko, and E. Park, “Compact 3d gaussian representation for radiance field,” in *Proceedings of the IEEE/CVF Conference on Computer Vision and Pattern Recognition (CVPR)*, 2024, pp. 21 719–21 728.

[72] S. Niedermayr, J. Stumpfegger, and R. Westermann, “Compressed 3d gaussian splatting for accelerated novel view synthesis,” in *2024 IEEE/CVF Conference on Computer Vision and Pattern Recognition (CVPR)*, 2024, pp. 10 349–10 358.

[73] M. Wu, Z. Wang, G. Kourous, and T. Tuytelaars, “Tetrrf: Temporal triplane radiance fields for efficient free-viewpoint video,” in *CVPR*, June 2024, pp. 6487–6496.

[74] B. Attal, J.-B. Huang, C. Richardt, M. Zollhoefer, J. Kopf, M. O’Toole, and C. Kim, “HyperReel: High-fidelity 6-DoF video with ray-conditioned sampling,” in *CVPR*, 2023.

[75] L. Li, Z. Shen, Z. Wang, L. Shen, and P. Tan, “Streaming radiance fields for 3d video synthesis,” *Advances in Neural Information Processing Systems*, vol. 35, pp. 13 485–13 498, 2022.

[76] Z. Wang, A. Bovik, H. Sheikh, and E. Simoncelli, “Image quality assessment: from error visibility to structural similarity,” *IEEE Transactions on Image Processing*, vol. 13, no. 4, pp. 600–612, 2004.

[77] B. S. Pateux and J. Jung, “An excel add-in for computing bjontegaard metric and its evolution,” in *vceg meeting*, 2007.